Available online at www.sciencedirect.com
SCIENCE DIRECT
Journal of Catalysis 241 (2006) 276–286
JOURNAL OF CATALYSIS
www.elsevier.com/locate/jcat

An investigation of the factors influencing the activity of $Cu/Ce_xZr_{1-x}O_2$ for methanol synthesis via CO hydrogenation

Konstantin A. Pokrovski, Alexis T. Bell *

Chemical Sciences Division, Lawrence Berkeley National Laboratory and Department of Chemical Engineering, University of California, Berkeley, CA 94720-1462, USA

Received 21 March 2006; revised 18 April 2006; accepted 5 May 2006

Available online 9 June 2006

Abstract

An investigation was carried out to identify the effects of incorporating Ce into ZrO_2 on the catalytic activity and selectivity of $Cu/Ce_xZr_{1-x}O_2$ for the hydrogenation of CO to methanol. A series of $Ce_xZr_{1-x}O_2$ solid solutions was synthesized by forced hydrolysis at low pH. The resulting catalysts were characterized to determine the structure of the mixed oxide phase, the H_2 and CO adsorption capacities of the catalyst, and the reducibility of both oxidation states of both Cu and Ce. The methanol synthesis activity goes through a maximum at $x = 0.5$, and the activity of 3 wt% $Cu/Ce_{0.5}Zr_{0.5}O_2$ catalyst is four times higher than that of 3 wt% Cu/ZrO_2 when tested at total pressure of 3.0 MPa and temperatures between 473 and 523 K with a feed containing H_2 and CO ($H_2/CO = 3$). The maximum in methanol synthesis activity is paralleled by a maximum in the hydrogen adsorption capacity of the catalyst, an effect attributed to the formation of Ce^{3+}–O(H)–Zr^{4+} species by dissociative adsorption of H_2 on particles of supported Cu followed by spillover of atomic H onto the oxide surface and reaction with Ce^{4+}–O–Zr^{4+} centers. In situ infrared spectroscopy shows that formate and methoxide groups are the primary adspecies present on $Cu/Ce_xZr_{1-x}O_2$ during CO hydrogenation. The rate-limiting step for methanol synthesis is the elimination of methoxide species by reaction with Ce^{3+}–O(H)–Zr^{4+} species. The higher concentration of Ce^{3+}–O(H)–Zr^{4+} species on the oxide surface, together with the higher Brønsted acidity of these species, appears to be the primary cause of the four-fold higher activity of 3 wt% $Cu/Ce_{0.5}Zr_{0.5}O_2$ relative to 3 wt% Cu/ZrO_2.
© 2006 Elsevier Inc. All rights reserved.

Keywords: Methanol; Cu; Zirconia; ZrO_2; Synthesis gas

1. Introduction

Zirconia-supported copper catalysts exhibit a high activity for the hydrogenation of CO to methanol, and can be used with or without the presence of CO_2 [1–7]. Mechanistic studies have shown that the active centers for methanol synthesis occur on the surface of the oxide, rather than the surface of the supported Cu particles [4]. CO adsorbs preferentially on the surface of zirconia to form formate species that then undergo hydrogenation to produce methanol. The hydrogen atoms required for this process are produced by dissociative adsorption of H_2 on the surface of the dispersed Cu and then spillover onto the zirconia surface. It has also been shown that the phase of zirconia influences catalyst activity. Thus, Cu/*m*-ZrO_2 (*m*-ZrO_2, monoclinic zirconia) was shown to be nearly an order of magnitude more active for methanol synthesis than Cu/*t*-ZrO_2 (*t*-ZrO_2, tetragonal zirconia) for equivalent zirconia surface areas and surface concentrations of dispersed Cu [6]. This difference is attributed primarily to the presence of oxygen vacancies on the surface of *m*-ZrO_2, which facilitate the reaction of CO with neighboring hydroxyl groups to generate formate species and provide additional sites for hydrogen activation and storage. These properties result in higher CO adsorption capacities and higher rates of elimination of methoxide species on Cu/*m*-ZrO_2 relative to Cu/*t*-ZrO_2. More recently, the effects of incorporating Ce into ZrO_2 on the catalytic performance of Cu/ZrO_2 for the hydrogenation of CO have been investigated [8]. The three-fold higher rate of methanol synthesis on 1.2 wt% $Cu/Ce_{0.3}Zr_{0.7}O_2$ relative to 1.2 wt% Cu/*m*-ZrO_2 was attributed to the higher surface concentration of H atoms on the former catalyst; however, a clear picture of how Ce incorporation into ZrO_2 increases

* Corresponding author.
E-mail address: alexbell@berkeley.edu (A.T. Bell).

0021-9517/$ – see front matter © 2006 Elsevier Inc. All rights reserved.
doi:10.1016/j.jcat.2006.05.002

the hydrogen adsorption capacity of the catalyst was not addressed.

The present study was undertaken to examine the influence of incorporating Ce into ZrO_2 on the catalytic activity of $Cu/Ce_xZr_{1-x}O_2$ for methanol synthesis from CO/H_2. $Ce_xZr_{1-x}O_2$ mixed oxides were prepared by forced hydrolysis at low pH, and Cu was dispersed on the surface of these materials by the deposition-precipitation technique. Catalysts were characterized by X-ray diffraction (XRD), Raman spectroscopy, XANES, and temperature-programmed reduction (TPR) in H_2, and the H_2 and CO adsorption capacities of each catalyst were measured by temperature-programmed desorption (TPD). Steady-state catalytic performance measurements were made, and transient-response in situ infrared studies were conducted to probe the reactivity of adsorbed species. These studies suggest that an important contributor to the higher methanol synthesis activity of $Cu/Ce_xZr_{1-x}O_2$ is the presence of $Ce^{4+}(O)Zr^{4+}$ centers at the catalyst surface. It is proposed that hydrogen adsorbs at these centers as $Ce^{3+}(OH)Zr^{4+}$. A maximum in the area-based activity of $Cu/Ce_xZr_{1-x}O_2$ occurs for $x = 0.5$, coinciding with the maximum H_2 adsorption capacity of the catalyst.

2. Experimental

2.1. Catalyst preparation

A series of $Ce_xZr_{1-x}O_2$ ($x = 0$, 0.1, 0.3, 0.5, 0.7, and 1.0) was prepared by boiling a 0.5 M (total metals basis) aqueous solution of zirconyl nitrate ($ZrO(NO_3)_2 \cdot xH_2O$, 99.99%, Aldrich) and cerium(III) nitrate ($Ce(NO_3)_3 \cdot 6H_2O$, 99.999%, Aldrich) under reflux for 240 h [6,8]. The final solutions had a pH < 1. NH_4OH was added dropwise to agglomerate the resulting fine particles and facilitate their filtration. The recovered precipitate was washed with deionized water. The washed solid was then dried in air overnight at 383 K. Each sample was calcined at 873 K in dry air flowing at 100 cm^3/min. The temperature was ramped from room temperature at a rate of 2 K/min to the final temperature, which was maintained for 3 h. Copper was then dispersed onto each support by deposition-precipitation [6] to obtain a series of 3 wt% $Cu/Ce_xZr_{1-x}ZrO_2$ catalysts.

2.2. Catalyst characterization

The crystallographic phase of $Ce_xZr_{1-x}O_2$ was determined by XRD and Raman spectroscopy. XRD patterns were obtained with a Siemens D5000 diffractometer, which uses Cu-K_α radiation and a graphite monochromator. Scans were made in the 2θ range of 20 to 90° with a step size of 0.02° and a time/step of 11 s. Raman spectra were recorded with a HoloLab 5000 Raman spectrometer (Kaiser Optical) at room temperature at a resolution of 2 cm^{-1}. The stimulating light source was a Nd:YAG laser, the output of which was frequency-doubled to 532 nm. Laser power at the sample was approximately 20 mW.

The BET surface area of each $Ce_xZr_{1-x}O_2$ support was determined using an Autosorb 1 (Quantachrome Instruments) gas adsorption system. Prior to each analysis, samples were dried at 393 K under vacuum for >2 h. BET surface areas were calculated using a five-point isotherm. After calcinations, the surface areas ranged from 80 to 140 m^2/g, as reported in Table 1. Within experimental error, identical BET areas were obtained for the catalysts after Cu deposition.

Hydrogen TPR studies were conducted using 0.15 g of a calcined sample, which had been purged with He at 298 K for 30 min. The flow was then switched from pure He to a 2% H_2/He mixture flowing at 60 cm^3/min, and temperature of the sample was ramped at 20 K/min from 298 to 673 K. The consumption of H_2 was monitored using a mass spectrometer (Cirrus, Spectra Products).

Cu K-edge and Ce L_{III}-edge XANES data were acquired at the Stanford Synchrotron Radiation Laboratory (SSRL) on beamline 2-3. Each sample was mixed with boron nitride and pressed into a rectangular pellet (0.43 × 1.86 cm) and loaded into an in situ cell for transmission experiments [9]. A sufficient quantity of each sample was used to give a calculated absorbance of 2.5. Each sample was calcined in 10% O_2/He at 573 K for 2 h, then cooled to 298 K, purged with He, and evacuated to 10^{-6} Torr to remove residual oxygen. A 2% H_2/He mixture was then passed through the cell at a flow rate of 60 cm^3/min. In situ XANES data at the Ce L_{III}-edge were acquired while the sample was heated from 298 K to 573 K at 4 K/min in a flow of 2% H_2/He (60 cm^3/min). Similar experiments were performed to acquire data at the Cu K-edge. XANES analyses were carried out using the Athena (version 0.8.041) software [10,11]. The energy was calibrated using the Ce L_{III}-edge of CeO_2 ($E_0 = 5728$ eV) and the Cu K-edge of a Cu foil ($E_0 = 8980$ eV). Pre-edge absorptions due to the background and detector were subtracted using a linear fit to the data in the range of −200 to −50 eV relative to the sample edge energy (E_0). Each spectrum was then normalized by a constant determined by the average absorption in the range of 100–300 eV relative to E_0. The edge energy of each sample

Table 1
Effect of oxide composition on the surface properties of 3 wt% $Cu/Ce_xZr_{1-x}O_2$

Catalyst	S.A. (m^2/g)	H_2 adsorption capacity ($\mu mol/m^2$)	CO adsorption capacity ($\mu mol/m^2$)	Ce^{3+}/Ce-total (%)
3 wt% Cu/ZrO_2	123	0.3	0.50	–
3 wt% $Cu/Ce_{0.1}Zr_{0.9}O_2$	138	1.16	0.60	32.97
3 wt% $Cu/Ce_{0.3}Zr_{0.7}O_2$	127	1.51	0.65	62.77
3 wt% $Cu/Ce_{0.5}Zr_{0.5}O_2$	83	3.06	1.43	60.81
3 wt% $Cu/Ce_{0.7}Zr_{0.3}O_2$	87	2.79	1.50	24.88
3 wt% Cu/CeO_2	53.7	2.31	1.58	15.19

and reference was taken at the first inflection point beyond any pre-edge peaks.

H_2 and CO adsorption capacities and were determined using TPD. For H_2, the sample was calcined and then reduced at 573 K in a 2% H_2/He mixture flowing at 60 cm^3/min. The sample was then cooled in 2% H_2/He to 298 K and purged in He. Desorption was conducted by ramping the sample temperature at 20 K/min from 298 to 773 K in flowing He (60 cm^3/min) while monitoring the desorbing gas using a mass spectrometer. To determine the CO adsorption capacity, the sample was calcined, then reduced in 2% H_2/He mixture flowing at 60 cm^3/min 573 K, cooled to 523 K, and flushed with He (60 cm^3/min) for 30 min. A 4.0% CO/He mixture was then passed over the catalyst for 60 min at a flow rate of 60 cm^3/min. The sample was then cooled to 298 K in a 4.0% CO/He mixture flowing AT 60 cm^3/min before it was purged for 30 min with He (60 cm^3/min) to remove any weakly adsorbed species. Desorption of adsorbed CO was carried out in a manner identical to that used for adsorbed H_2.

2.3. Catalyst testing

Activity and selectivity measurements for CO hydrogenation were carried out in a glass-lined stainless-steel reactor as described previously [6]. Before testing, each catalyst was calcined in a 10% O_2/He mixture flowing at 60 cm^3/min. The sample was heated from room temperature to 573 K at 0.5 K/min and maintained at 573 K for 2 h, then cooled to 323 K, and swept with He. Finally, the sample was reduced in a 10% H_2/He mixture flowing at 60 cm^3/min while the temperature was increased at a rate of 2 K/min up to 573 K. The flow of 10% H_2/He was maintained at 573 K for 1 h before switching to a flow of 100% H_2 for an additional 1 h. Reactions were carried out with 0.15 g of catalyst at a total pressure of 3.0 MPa. Total reactant gas flow was 60 cm^3/min (at STP) with a H_2/CO ratio of 3/1. Product gas mixtures were analyzed after 2 h on stream at a given temperature. The temperature was then ramped to the next highest temperature at a rate of 2 K/min and maintained there for 2 h. Conversion and selectivity were referenced to the consumption of CO, the limiting reactant.

2.4. Infrared spectroscopy studies

In situ transmission infrared spectroscopy experiments were conducted using a low dead-volume infrared cell equipped with CaF_2 windows [12]. To remove any residual surface species before testing, each sample was calcined in a 10% O_2/He mixture flowing at 60 cm^3/min. The sample was heated from room temperature to 523 K at a rate of 2 K/min and then there for 8 h. The sample was then cooled to 323 K, swept with He, and reduced in a 10% H_2/He mixture flowing at 60 cm^3/min while the temperature was increased at a rate of 2 K/min up to 523 K. The flow of 10% H_2/He was maintained at 523 K for 1 h before switching to a flow of 100% H_2 for an additional 1 h. The sample was then flushed with He for 1 h before sample testing. Carbon monoxide adsorption and hydrogenation experiments were carried out at a total pressure of 0.5 MPa.

3. Results

3.1. Material characterization of $Ce_xZr_{1-x}O_2$ supports

XRD patterns of the $Ce_xZr_{1-x}O_2$ materials are shown in Fig. 1a. The principal features seen in the diffraction pattern can be ascribed to tetragonal ZrO_2 (t-ZrO_2), with only a trace of monoclinic ZrO_2 (m-ZrO_2) evident at 28.2°. The volume fraction of m-ZrO_2 was estimated to be ∼0.2 using the relationships [13]

$$V_m = \frac{1.311X_m}{1 + 0.311X_m}$$

and

$$X_m = \frac{I_m(111) + I_m(11\bar{1})}{I_m(111) + I_m(11\bar{1}) + I_t(111)},$$

where $I_m(111)$ and $I_m(11\bar{1})$ are the line intensities of the (111) and $(11\bar{1})$ peaks for m-ZrO_2 and $I_t(111)$ is the intensity of the (111) peak for t-ZrO_2. The diffraction peaks shifted to lower values of 2Θ on introduction of Ce into ZrO_2, consistent with an increase in the lattice cell parameter on the substitution of Zr^{4+} (radius 0.86 Å) by Ce^{4+} cations (radius, 0.97 Å). $Ce_xZr_{1-x}O_2$ with $x = 0.5$ and 0.7 showed a small degree of

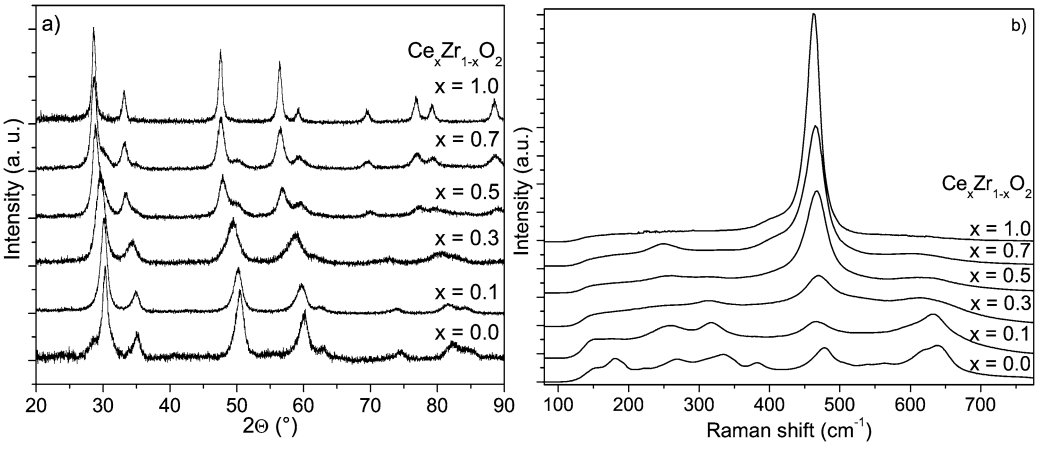

Fig. 1. XRD patterns (a) and Raman spectra (b) of $Ce_xZr_{1-x}O_2$.

phase segregation into cerium-rich and zirconium-rich phases, as evidenced by the appearance of XRD peaks at ∼28.7° and a shoulder at ∼30.0°, respectively [14].

Each material was also characterized by Raman spectroscopy. Fig. 1b shows Raman spectra of $Ce_xZr_{1-x}O_2$ collected at 298 K. Pure ZrO_2 exhibited peaks at 153, 181, 270, 335, 385, 478, 615, and 640 cm^{-1}. The peak at 188 cm^{-1} is characteristic of the monoclinic zirconia, whereas the peaks at 153 and 270 cm^{-1} are due to the tetragonal phase [15–17]. Thus, Raman spectroscopy confirmed the presence of tetragonal ZrO_2, but also revealed the existence of a significant amount of monoclinic ZrO_2. However, neither XRD nor visible Raman spectroscopy could provide insight into the relative location of the *m*- and *t*-ZrO_2 phases, because both techniques sample the particles of ZrO_2 uniformly. Work by Li and Li [17] using XRD, visible Raman spectroscopy, and UV–Raman spectroscopy has demonstrated that the transformation of *t*-ZrO_2 to *m*-ZrO_2 occurs initially at the surface of the ZrO_2 particles. *m*-ZrO_2 could be detected at lower calcination temperatures by UV–Raman spectroscopy compared with either visible Raman spectroscopy or XRD, due to the higher surface sensitivity of UV–Raman spectroscopy relative to visible Raman spectroscopy. Therefore, the difference in the identity of the predominant phase of ZrO_2 determined using XRD and Raman spectroscopy is very likely due to the presence of a layer of *m*-ZrO_2 on the surface of bulk *t*-ZrO_2 particles. Further support for this picture was obtained from infrared spectra of the O–H stretching region, as discussed below.

The Raman spectrum of $Ce_{0.1}Zr_{0.9}O_2$ (Fig. 1b) exhibited peaks at 149, 265, 319, 468, and 633 cm^{-1}, attributed to the tetragonal phase of zirconia [15–17]. The XRD pattern also confirms the tetragonal structure of $Ce_{0.1}Zr_{0.9}O_2$ (Fig. 1a). The position of the 111 XRD peak for $Ce_{0.1}Zr_{0.9}O_2$ shifted to a lower value of 2Θ (30.1°) relative to that for pure *t*-ZrO_2 (30.3°). Thus, the introduction of 10 at% cerium into zirconia clearly stabilized the tetragonal phase. Increasing the cerium content to 30 at% shifted the 111 XRD peak to 29.5°. The broad diffraction peaks for $Ce_{0.3}Zr_{0.7}O_2$ make it impossible to definitively distinguish between tetragonal and cubic phases of this material. The Raman spectrum of $Ce_{0.3}Zr_{0.7}O_2$, presented in Fig. 1b, shows a principle peak at 469 cm^{-1} and two smaller peaks at 320 and 620 cm^{-1}. The peak at 469 cm^{-1} is characteristic of a cubic fluorite structure [18–20]. However, the presence of peaks at 320 and 620 cm^{-1} (due to tetragonal distortion of oxygen sub lattice) and the absence of the characteristic tetragonal peak at ∼270 cm^{-1} indicate that $Ce_{0.3}Zr_{0.7}O_2$ is in the t″ phase [20]. This phase is intermediate between the tetragonal and cubic phases, in which the oxygen atoms are displaced from the positions of these atoms in an ideal fluorite structure. Although the t″ phase is commonly reported to exist at Ce compositions between 65 and 80 at% [20], other authors have reported the generation of this phase at lower Ce content for small particles [21,22].

The Raman spectra of $Ce_{0.5}Zr_{0.5}O_2$ and $Ce_{0.7}Zr_{0.3}O_2$ exhibited a principle peak at 467 cm^{-1} and smaller peaks at 254, 315, and 625 cm^{-1}. The peak at 465 cm^{-1} is characteristic of a cubic fluorite structure, whereas the peaks at 254, 315, and 625 cm^{-1} can be assigned to the tetragonal phase [18–20]. Comparison of the XRD patterns and Raman spectra for $Ce_{0.5}Zr_{0.5}O_2$ and $Ce_{0.7}Zr_{0.3}O_2$ suggests that these materials contain two phases, a cubic (cerium-rich) phase and a tetragonal (zirconium-rich) phase. Raman spectrum of pure ceria exhibited a single peak at 463 cm^{-1} characteristic of the cubic phase [18–20].

3.2. Characterization of $Cu/Ce_xZr_{1-x}O_2$

Fig. 2 presents TPR profiles of 3 wt% $Cu/Ce_xZr_{1-x}O_2$. The 3 wt% Cu/ZrO_2 exhibited a principle peak centered at 455 K, attributed to the reduction of highly dispersed CuO [23,24]. The amount of H_2 consumed was slightly greater than the value corresponding to the complete reduction of CuO ($H_2/CuO \approx 1.1$), in good agreement with previous reports [6]. The 3 wt% $Cu/Ce_xZr_{1-x}O_2$ ($x > 0$) samples exhibited a significantly greater-than-expected H_2 consumption for the reduction of CuO, suggesting that some of the Ce^{4+} underwent reduction to Ce^{3+}. The appearance and interpretation of the observed TPR spectra are similar to those reported for $CuO/Ce_{0.44}Zr_{0.56}O_2$ [25].

In situ XANES experiments were conducted to determine the degree of Cu and Ce reduction. As shown in Fig. 3a, Cu K-edge XANES demonstrates that the reduction of Cu was complete after the samples were heated in 2% H_2/He at 573 K for 1 h. Ce L_{III}-edge XANES spectra collected after the H_2 reduction of 3 wt% $Cu/Ce_xZr_{1-x}O_2$ are presented in Fig. 3b. Comparing these spectra with those of $Ce_2(SO_4)_3$ and CeO_2 shows that both Ce^{4+} and Ce^{3+} were present after reduction. The distribution between these two oxidation states of Ce was calculated using a linear combination fitting of Ce^{3+} and Ce^{4+} standards in Athena [10,11]; the results are given in Table 1. The maximum of reduction of Ce^{4+} to Ce^{3+} was observed for 3 wt% $Cu/Ce_{0.3}Zr_{0.7}O_2$ and 3 wt% $Cu/Ce_{0.5}Zr_{0.5}O_2$. These results are consistent with findings of previous studies of $Ce_xZr_{1-x}O_2$ [26–28] showing that the introduction of zirconium into ceria increased the reducibility of Ce^{4+} due to increased oxygen mobility for oxides with intermediate Ce/Zr ratios.

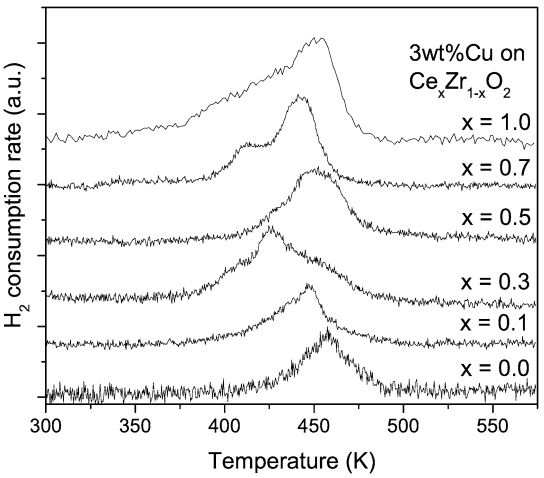

Fig. 2. H_2-TPR spectra for 3 wt% $Cu/Ce_xZr_{1-x}O_2$. Heating rate, 20 K/min; 2% H_2/He flow rate, 60 cm^3/min.

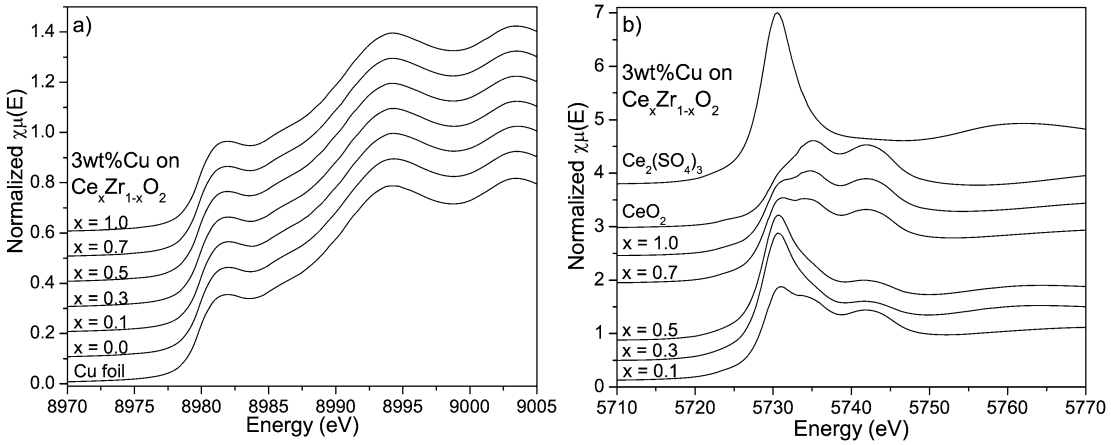

Fig. 3. XANES spectra of 3 wt% Cu/$Ce_{0.3}Zr_{0.7}O_2$ at (a) Cu K-edge and (b) Ce L_{III}-edge reduction in 2% H_2/He at 573 K for 1 h.

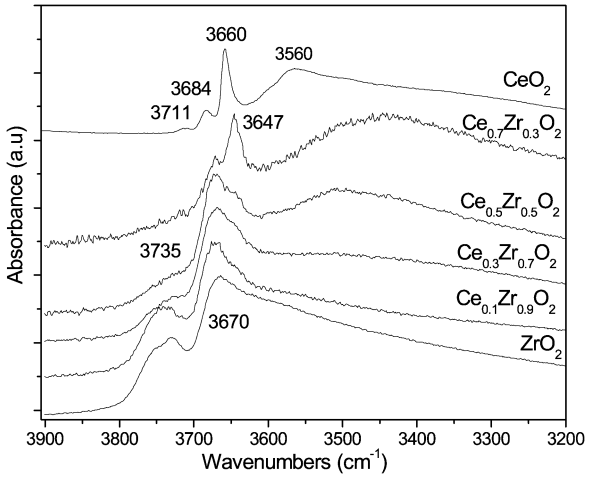

Fig. 4. Infrared spectra of the hydroxyl group stretching region taken for 3 wt% Cu/$Ce_xZr_{1-x}O_2$ following calcination and reduction. Spectra referenced to empty cell in He.

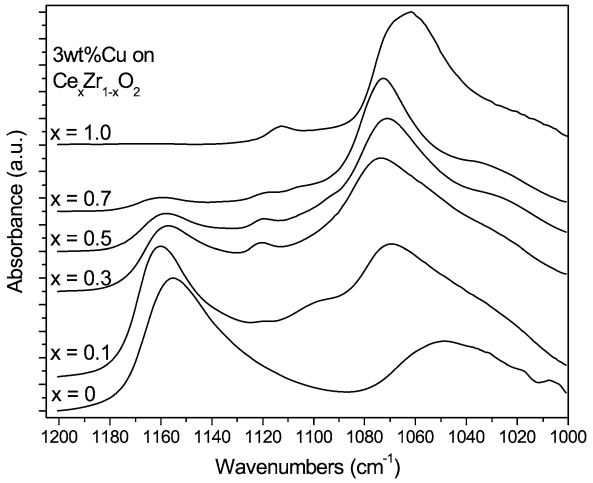

Fig. 5. Infrared spectra of the C–O stretching region of surface methoxide groups taken in 0.5% CH_3OH/He flow at 523 K. Spectra referenced to the samples under He flow at 523 K.

The infrared spectra of the O–H stretching region obtained after reduction at 523 K are shown in Fig. 4. Spectra were referenced to the empty cell filled with He. Peak intensities were normalized to account for slight differences in the weights of each sample. The positions of these bands are similar to those reported previously for ZrO_2 and CeO_2 [29–31]. Surface hydroxyl groups on ZrO_2 and CeO_2 are commonly assigned based on the number of coordinating cations, with the higher-frequency species representing terminal groups and the lower-frequency species representing either bi- or tri-bridging groups [29–31]. The peak positions for ZrO_2 (3666 and 3731 cm^{-1}) more closely resemble those observed for *m*-ZrO_2 (3668 and 3729 cm^{-1}) than those of *t*-ZrO_2 (3660 and 3738 cm^{-1}) [6]. Similar to *m*-ZrO_2, the ZrO_2 sample exhibited a higher relative concentration of the low-frequency band (at 3666 cm^{-1}), suggesting that the ZrO_2 particles contain a significant fraction of *m*-ZrO_2 at their surface. The infrared spectrum of reduced CeO_2 exhibited three absorption bands in the OH stretching region at 3710 (terminal, I), 3684 (bridged, IIA), 3655 (bi-bridged, IIB), and 3560 cm^{-1} (tri-briged, III) [30,31]. The introduction of Ce into zirconia increased the relative concentration of bridging hydroxyl groups, and these species became dominant for Ce content >30 at%. The OH stretching band due to the bridging hydroxyl group (IIB) bonded to Ce^{3+} cations is evident at 3647 cm^{-1} in the infrared spectra of mixed oxides [30,31].

The nature of surface species formed on adsorption of methanol was characterized using in situ infrared spectroscopy. Fig. 5 shows spectra obtained on reduced 3 wt% Cu/$Ce_xZr_{1-x}O_2$ obtained at 523 K during sample exposure to a flow of 0.5% CH_3OH/He at a total pressure of 0.50 MPa. The peaks at 1150–1160 and 1112–1120 cm^{-1} are assigned to C–O stretching vibrations of terminal methoxide species (*t*-OCH_3) bonded to Zr^{4+} and Ce^{3+} cations, respectively [32,33]. The absence of a band at 1105 cm^{-1} for terminal methoxide species bonded to Ce^{4+} cations [32,33] suggests that all of the Ce^{4+} present at the surface of the 3 wt% Cu/$Ce_xZr_{1-x}O_2$ was reduced to Ce^{3+} during reduction of the samples in H_2 at 523 K before being exposed to methanol. As the cerium concentration in the support increased, the relative intensity of peak at 1155 cm^{-1} decreased and the intensity of the peak at 1115 cm^{-1} increased. The broad band centered at 1050–1075 cm^{-1} is assigned to C–O stretch-

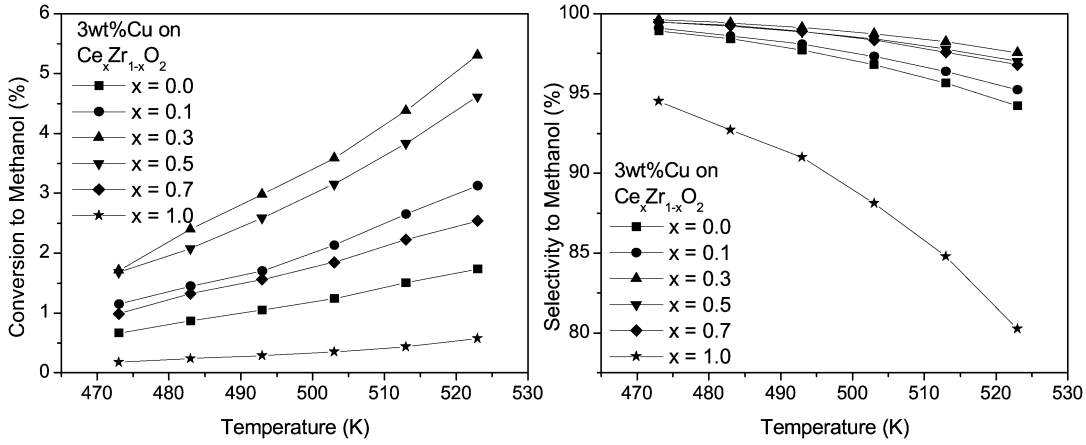

Fig. 6. Effect of temperature on the selective conversion and overall selectivity of CO to methanol during CO hydrogenation: catalyst mass, 0.15 g; $P = 3.0$ MPa; $H_2/CO = 3$; total flow rate, 60 cm^3/min.

Table 2
Effect of oxide composition on the activity of 3 wt% Cu/$Ce_xZr_{1-x}O_2$ for CO hydrogenation

Catalyst	Conversion (selectivity) at 523 K (%)	Productivity ($g_{CH_3OH}\ g_{cat}^{-1}\ h^{-1}$)	Productivity ($mg_{CH_3OH}\ m^{-2}\ h^{-1}$)
3 wt% Cu/ZrO_2	1.73 (94.23)	0.136	1.10
3 wt% Cu/$Ce_{0.1}Zr_{0.9}O_2$	3.12 (95.24)	0.245	1.78
3 wt% Cu/$Ce_{0.3}Zr_{0.7}O_2$	5.30 (97.57)	0.416	3.28
3 wt% Cu/$Ce_{0.5}Zr_{0.5}O_2$	4.61 (97.02)	0.362	4.36
3 wt% Cu/$Ce_{0.7}Zr_{0.3}O_2$	2.54 (96.80)	0.199	2.29
3 wt% Cu/CeO_2	0.57 (79.78)	0.025	0.46

Catalyst mass, 0.15 g; $T = 523$ K; $P = 3.0$ MPa; $H_2/CO = 3$; total flow rate, 60 cm^3/min.

ing vibrations of bridge-bonded methoxide species (*b*-OCH_3) [32,33]. The position of this peak shifted from 1045 cm^{-1} for 3 wt% Cu/ZrO_2 to 1072 cm^{-1} for 3 wt% Cu/$Ce_{0.7}Zr_{0.3}O_2$. This trend suggests that with increasing Ce content, the fraction of Ce^{3+} in the pairs and triads of metal cations involved in bridge-bonded methoxide species increased. The decreased intensity of the infrared bands in the OH stretching region on adsorption of methanol indicates that surface methoxide species were formed by interaction of gas-phase methanol with surface OH groups. The increased relative concentration of bridged CH_3O species with increased Ce content is consistent with the increased concentration of bridged hydroxyl groups (Figs. 4 and 5). The spectrum of methanol adsorbed on 3 wt% Cu/CeO_2 reduced at 523 K exhibited C–O stretching modes at 1112 (terminal, I), 1072 (bi-bridged, IIA), 1061 (bi-bridged, IIB), and 1030 cm^{-1} (tribriged, III). The peak positions are consistent with the values reported by Binet and Daturi [33].

The H_2 and CO adsorption capacities of 3 wt% Cu/$Ce_xZr_{1-x}O_2$ determined from TPD spectra are listed in Table 1. The amount of CO adsorbed per unit area increased monotonically with increasing cerium content. In contrast, the amount of H_2 adsorbed goes through the maximum at $Ce/Zr = 1$. Desorption of H_2 was observed in the temperature range of 320–680 K and was not accompanied by the release of water. The latter observation suggests that hydrogen desorption occurred via the decomposition of surface hydroxyl groups formed on reduction in H_2, as shown below:

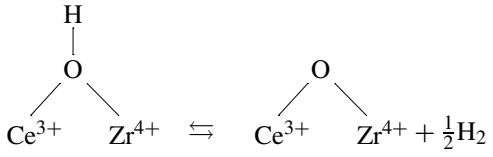

3.3. Catalytic performance of Cu/$Ce_xZr_{1-x}O_2$

The effects of reaction temperature on the activity and selectivity of the 3 wt% Cu/$Ce_xZr_{1-x}O_2$ catalysts are illustrated in Fig. 6. The conversion of CO to methanol increased over the temperature range of 473–523 K, accompanied by decreased methanol selectivity. The only major byproduct observed was methane. Because the measured conversion levels were far below those expected for equilibrium at the conditions used here, the observed rates of methanol formation were not influenced by the rates of methanol decomposition. The steady-state activities of 3 wt% Cu/$Ce_xZr_{1-x}O_2$ for methanol synthesis are presented in Table 2. The methanol productivity of 3 wt% Cu/$Ce_xZr_{1-x}O_2$ reached a maximum versus Ce content. The most active catalyst based on catalyst weight was 3 wt% Cu/$Ce_{0.3}Zr_{0.7}O_2$ (0.42 $g_{CH_3OH}\ g_{cat}^{-1}\ h^{-1}$), but the most active catalyst based on catalyst surface area was 3 wt% Cu/$Ce_{0.5}Zr_{0.5}O_2$ (4.36 $mg_{CH_3OH}\ m^{-2}\ h^{-1}$).

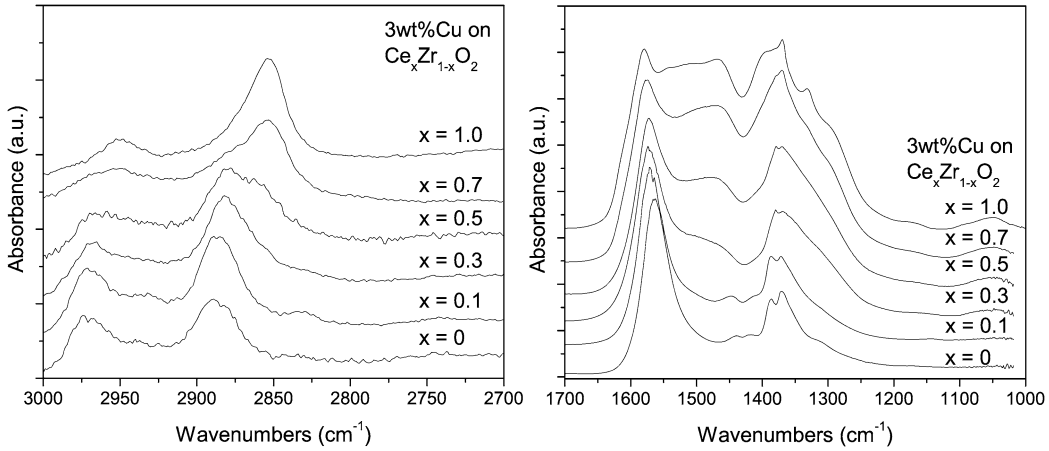

Fig. 7. Infrared spectra taken for 3 wt% Cu/Ce$_x$Zr$_{1-x}$O$_2$ at 523 K in 0.05 MPa CO and 0.45 MPa He flowing at a total rate of 60 cm^3/min. Spectra referenced to 3 wt% Cu/Ce$_x$Zr$_{1-x}$O$_2$ under 0.50 MPa He flow at 523 K.

3.4. Infrared spectroscopy studies

The nature of surface species and the dynamics of CO adsorption and hydrogenation were studied using in situ infrared spectroscopy. Fig. 7 shows spectra obtained during CO adsorption on 3 wt% Cu/Ce$_x$Zr$_{1-x}$O$_2$ catalysts previously reduced in H_2 at 523 K. Spectra were collected at 523 K after the catalyst had been exposed to a flow of 15% CO/He at a total pressure of 0.50 MPa for 1 h. For the 3 wt% Cu/ZrO_2 sample, the bands observed at 1563, 1386, and 1369 cm^{-1} are attributable to the ν_{as}(OCO), δ(CH), and ν_s(OCO) modes, respectively, of *b*-HCOO–Zr [32–35]. Accompanying features for *b*-HCOO–Zr in the CH stretching region occurred at 2969 and 2888 cm^{-1}, characteristic of (ν_{as}(OCO) + δ(CH)) [32–35] and ν_s(CH) [32–35], respectively. Weak features at 2934 and 2832 cm^{-1} attributed to CH_3O–Zr [32–35] appeared even in the absence of gas phase H_2. Weak bands at 1155 and 1040 cm^{-1} are assigned to C–O stretching vibrations of terminal (*t*-OCH_3) and bridged (*b*-OCH_3) methoxide species on ZrO_2, respectively; the shoulder located at approximately 1320 cm^{-1} is assigned to *b*-CO_3^{2-}–Zr species [32–35]. The peaks at 1440–1420 cm^{-1} can be attributed to various carbonate and carboxylate species on the surface of ZrO_2 [32–35]. Formate species adsorbed on 3 wt% Cu/CeO_2 sample are characterized by absorption bands at 2950 (ν_{as}(OCO) + δ(CH)), 2852 ν_s(CH), 1575 ν_{as}(OCO), 1380 (δ(CH)), and 1369 cm^{-1} (ν_s(OCO)) [32–35]. These bands are attributed to the bidentate formate species adsorbed on Ce^{3+} cations. Broad features at ∼1550–1450 and 1350–1250 cm^{-1} in the infrared spectrum of CO adsorbed on the 3 wt% Cu/CeO_2 sample are attributed to various carbonate and carboxylate species [32–35]

The infrared spectra of CO adsorbed on 3 wt% Cu/Ce$_x$Zr$_{1-x}$O$_2$ were qualitatively similar to those for 3 wt% Cu/ZrO_2 and 3 wt% Cu/CeO_2. With increasing Ce content, the shoulders at 2951 and 2854 cm^{-1}, assigned to bidentate formate species adsorbed on Ce^{3+} cations [25], increased in intensity. The relative concentration of methoxide species features (bands at 1155, 1050, 2935, and 2831 cm^{-1}) also increased with increasing cerium content. The presence of Ce in the catalyst increased the intensities of broad features between ∼1550–1450 and 1350–1250 cm^{-1} indicative of various carbonate and carboxylate species [36].

After CO adsorption for 1 h, H_2 was introduced into the flowing 15% CO/He mixture (total pressure, 0.50 MPa) so as to achieve a H_2/CO ratio of 3/1. Fig. 8 shows spectra obtained on 3 wt% Cu/Ce$_x$Zr$_{1-x}$O$_2$ at steady state after 6 h of exposure to a H_2/CO mixture at 523 K. The band at 1147 cm^{-1} is assigned to the ν(CO) mode of *t*-CH_3O species adsorbed on Zr^{4+}. Peaks corresponding to C–O stretching vibrations of *b*-CH_3O species were present at 1040–1064 cm^{-1}. The blue shift of the ν(CO) band for *b*-CH_3O species with increasing cerium content was similar to that observed in the spectra of adsorbed methanol (Fig. 6), suggesting that some CH_3O species were bonded to both Zr^{4+} and Ce^{3+} cations. The intensities of the bands for *b*-HCOO appearing at 1576, 1386, and 1366 cm^{-1} decreased relative to those observed on adsorption of CO (Fig. 7). In the C–H stretching region, bands for CH_3O species were present at 2926–2920 and 2822 cm^{-1}. The shoulders at 2970 and 2880 cm^{-1} are attributable to *b*-HCOO species. Similar to the peak at 1576 cm^{-1}, the intensities of the peaks at 2970 and 2880 cm^{-1} decreased with increasing cerium content. The band at 2796 cm^{-1} attributed to methoxy species adsorbed on Ce^{3+} cations increased in intensity with increasing cerium content. The δ(CH) feature for CH_3O was evident at 1446 cm^{-1} but was very weak in intensity [32–35]. The broad features between ∼1550–1450 and 1350–1250 cm^{-1} attributed to various carbonate and carboxylate species were similar to those observed during the adsorption of CO (Fig. 7). A red shift of the peak at 1070–1061 cm^{-1} (observed during methanol adsorption on reduced 3 wt% Cu/CeO_2) to 1053 cm^{-1} and the appearance of the band at 1090 cm^{-1} observed during CO hydrogenation suggests that Ce^{4+} species were formed on reduction of formate to methoxide species [32–35].

The relative rates of consumption of formate and methoxide species were evaluated by switching from a CO/H_2 mixture to one containing only H_2. Fig. 9a shows spectra of 3 wt% Cu/$Ce_{0.3}Zr_{0.7}O_2$ collected at the beginning of the transient experiment. The intensities of bands corresponding to *b*-HCOO and CH_3O species decreased after the feed was switched from

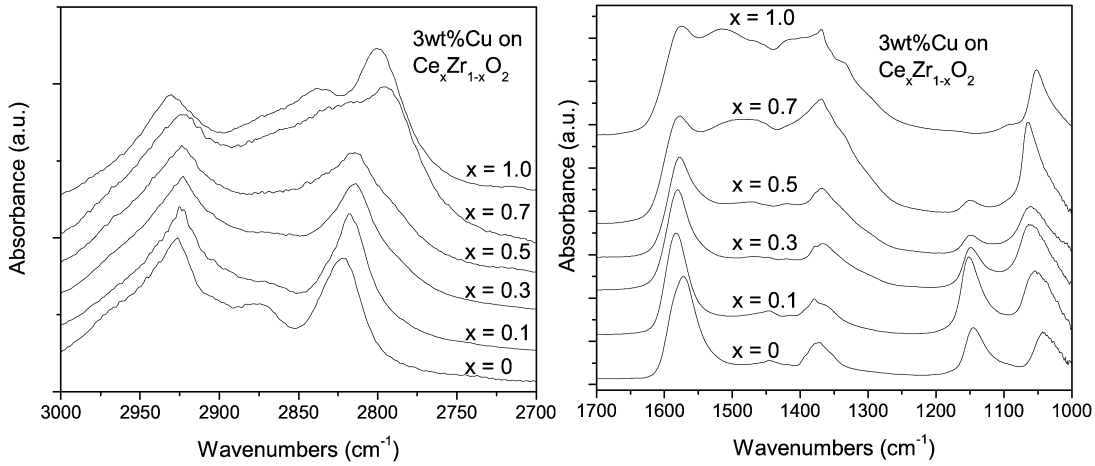

Fig. 8. Infrared spectra taken for 3 wt% Cu/$Ce_xZr_{1-x}O_2$ at 523 K in 0.05 MPa CO, 0.15 MPa H_2, and 0.30 MPa He flowing at a total rate of 60 cm^3/min. Spectra referenced to 3 wt% Cu/$Ce_xZr_{1-x}O_2$ under 0.50 MPa He flow at 523 K.

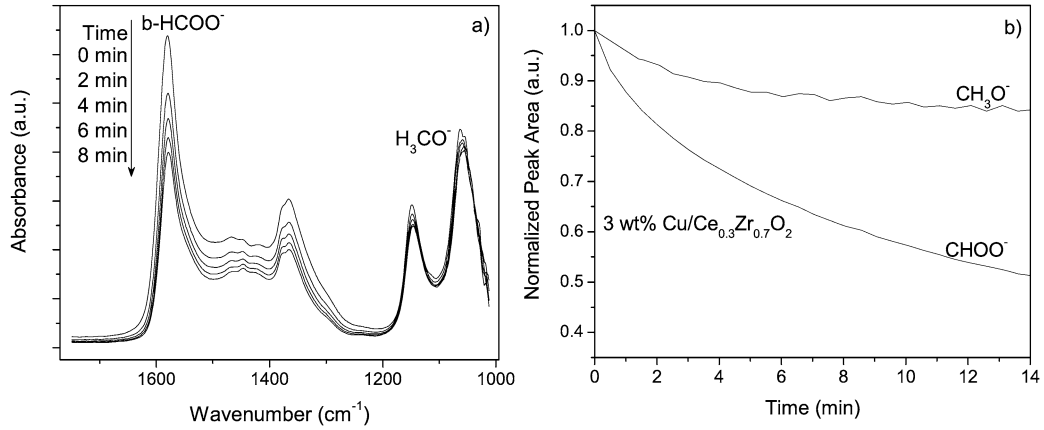

Fig. 9. (a) Infrared spectra taken for 3 wt% Cu/$Ce_{0.3}Zr_{0.7}O_2$ at 523 K after switching feed from 0.05 MPa CO, 0.15 MPa H_2, and 0.30 MPa He to 0.15 MPa H_2 and 0.35 MPa He flowing at a total rate of 60 cm^3/min. (b) Peak areas of *b*-HCOO$^-$ and CH_3O^- features for 3 wt% Cu/$Ce_{0.3}Zr_{0.7}O_2$ at 523 K after switching feed from 0.05 MPa CO, 0.15 MPa H_2, and 0.30 MPa He to 0.15 MPa H_2 and 0.35 MPa He flowing at a total rate of 60 cm^3/min. Areas normalized to the values observed at the beginning of the transient.

a H_2/CO/He mixture to a H_2/He mixture. The evolution of peak areas of formate and methoxide species is presented in Fig. 9b. Peak areas for both *b*-HCOO and CH_3O were normalized to the value observed at the beginning of the transient. In agreement with previous reports [7,8], the intensity of b-HCOO band decreased more rapidly from the intensities of the bands for methoxide species. These observations are consistent with the results of Bell and coworkers [7,8] and indicate that the rate-limiting step of methanol synthesis from H_2/CO was the elimination of surface methoxide species. To investigate the effect of cerium content on the rate of surface methoxide elimination, transient response experiments were performed for all 3 wt% Cu/$Ce_xZr_{1-x}O_2$ catalysts studied in this work.

Fig. 10 compares the dynamics of CHOO and CH_3O consumption on 3 wt% Cu/$Ce_xZr_{1-x}O_2$. Transient-response spectra were obtained by replacing the 15% CO/He in the 3/1 H_2/CO flow with He while maintaining the total pressure at 0.50 MPa. The integrated peak areas at 1600–1500 cm^{-1} for HCOO species and 1200–1000 cm^{-1} for CH_3O species were normalized to the value observed at the beginning of the transient. With increasing Ce content, the rates of CHOO and CH_3O consumption increased up to a maximum for $x = 0.5$, and then decreased. The rate of CHOO hydrogenation to methoxide was much higher then the rate of methoxide elimination regardless of catalyst composition, indicating that the rate-determining

Table 3
Effect of oxide composition on the apparent rate constant of 3 wt% Cu/$Ce_xZr_{1-x}O_2$ for CO hydrogenation

Catalyst	$k_{app} \times 10^{-3}$ (min^{-1})	$k_{app} \times C_{CH_3O}$ (a.u.)
3 wt% Cu/ZrO_2	5.8	1.1
3 wt% Cu/$Ce_{0.1}Zr_{0.9}O_2$	6.5	1.61
3 wt% Cu/$Ce_{0.3}Zr_{0.7}O_2$	18.1	3.67
3 wt% Cu/$Ce_{0.5}Zr_{0.5}O_2$	22.9	4.165
3 wt% Cu/$Ce_{0.7}Zr_{0.3}O_2$	12.2	2.55
3 wt% Cu/CeO_2	3.8	0.35

$T = 523$ K; 0.15 MPa H_2, 0.05 MPa CO, $P_{tot} = 0.5$ MPa; total flow rate, 60 cm^3/min. Values of $k_{app} \times C_{CH_3O}$ are normalized to the value of 1.1 for 3 wt% Cu/ZrO_2.

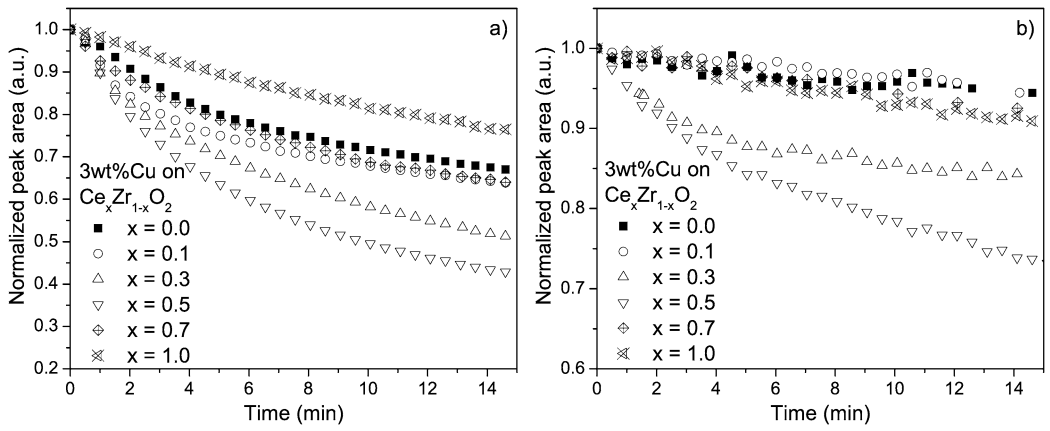

Fig. 10. Peak areas of (a) formate and (b) methoxide features for 3 wt% Cu/$Ce_xZr_{1-x}O_2$ at 523 K after switching feed from 0.05 MPa CO, 0.15 MPa H_2, and 0.30 MPa He to 0.15 MPa H_2 and 0.35 MPa He flowing at a total rate of 60 cm^3/min. Areas normalized to the values observed at the beginning of the transient.

step did not change with catalyst composition. The apparent first-order rate constant for the removal of methoxide species, k_{app}, determined from the initial portion of the transient is presented in Table 3. Here too, it is observed that k_{app} passed through a maximum for $x = 0.5$ in a manner similar to the steady-state activity per unit surface area given in Table 2. It is important to note, however, that the integrated band intensity for methoxide species (terminal and bridging) was little affected by the Ce content of the catalyst, even though the distribution between linear and bridging methoxide species changed with Ce content. However, as shown in Fig. 9, both types of methoxide species appeared to react at the same rate, likely due to a rapid interconversion between the bridging and terminal forms.

4. Discussion

The results of the present study are fully consistent with those reported by Pokrovski et al. [8] comparing the activity and selectivity of 1.2 wt% Cu/$Ce_{0.3}Zr_{0.7}O_2$ and 1.2 wt% Cu/ZrO_2. In that study, the ratio of surface area-based activities for the two catalysts was 3 times greater in favor of the Ce-containing catalyst, and the ratio of values of k_{app} was 2.4 for the Ce-containing catalyst. Based on an analysis of the transient-response spectra, Pokrovski et al. concluded that hydrogenation of methoxide species adsorbed on the oxide surface was the rate-determining step. Because the surface concentration of methoxide species was only 1.3 times greater for the Ce-containing catalyst, the higher activity of this catalyst was attributed to its higher adsorbed hydrogen content. Consistent with this reasoning, the measured ratio of hydrogen adsorption capacities at 523 K was reported to be 3.3 in favor of the Ce-containing catalyst. Although no physical reason for the higher adsorption capacity of the Ce-containing catalyst was proposed, it was suggested that this effect may have been related to the ability of Ce–O bonds at the oxide surface to stabilize H atoms as $H^{\delta-}$ and $H^{\delta+}$ species [8,37,38].

The results of the present investigation demonstrate that the effects of Ce content on the methanol synthesis activity and the hydrogen adsorption capacity of Cu/$Ce_xZr_{1-x}O_2$ were not monotonic but in fact varied in a similar fashion, both passing through a maximum at $x = 0.5$. The Ce L_{III}-edge XANES data also indicate that the extent of reduction of Ce^{4+} to Ce^{3+} also passed through a maximum for $x = 0.3$–0.5, but infrared spectra of adsorbed methanol (Fig. 4) suggest that the Ce cations present on the surface of the reduced catalyst were exclusively Ce^{3+}. This observation, together with the absence of water formation on the desorption of adsorbed H_2, led to the proposal (see above) that hydrogen was adsorbed on the oxide surface as Ce^{3+}–O(H)–Zr^{4+} and that these species were converted to Ce^{4+}–O–Zr^{4+} on H_2 desorption. Because no evidence for hydridic H was found by infrared spectroscopy, it appears that the increased adsorption of hydrogen on the surface of Cu/$Ce_xZr_{1-x}O_2$ was due not to the heterolytic dissociation of H_2 as proposed by Pokrovski et al. [8], but rather to the migration of H atoms spilled over from the surface of the dispersed Cu particles and their reaction with Ce^{4+}–O–Zr^{4+} pairs to form Ce^{3+}–O(H)–Zr^{4+}. Assuming a uniform mixing of Ce and Zr in the oxide phase, it thus seems reasonable to conclude that the highest concentration of Ce^{3+}–O(H)–Zr^{4+}, and hence the highest level of H_2 adsorption, occurred when $x = 0.5$, in agreement with previous observations. We also note that hydrogen can be stored on the surface of ZrO_2 in the form of Zr^{4+}–O(H)–Zr^{4+}. Such structures are likely to form only in the vicinity of O anion defects in the surface, because Zr^{4+} does not undergo reduction to Zr^{3+}. A further point of note is that protons present as Ce^{3+}–O(H)–Zr^{4+} would be expected to be more Brønsted-acidic, and hence more reactive toward anionic species, such as formates and methoxides, compared with protons present as Zr^{4+}–O(H)–Zr^{4+}.

Comparing the spectra of CH_3O species present on reduced catalysts (Fig. 5) and those present during CO hydrogenation (Fig. 8) suggests that under our reaction conditions, some of the surface Ce^{3+} cations were oxidized to Ce^{4+}. Based on the foregoing considerations, we propose that the effect of Ce cations on the activity of 3 wt% Cu/$Ce_xZr_{1-x}O_2$ for methanol synthesis can be interpreted in terms of the reaction sequence shown in Scheme 1. H_2 adsorbs on the surface of reduced Cu and spills over onto the surface of $Ce_xZr_{1-x}O_2$, where it reacts with Ce^{4+}–O–Zr^{4+} centers to form Ce^{3+}–O(H)–Zr^{4+} species. Previous studies have shown that Cu enhances the rate of H/D ex-

change of hydroxyl groups on the surface of Cu/ZrO_2 and that $Cu/Ce_{0.3}Zr_{0.7}O_2$ has a higher adsorption capacity than Cu/ZrO_2 [8,39]. As noted earlier, Ce^{3+}–O(H)–Zr^{4+} species are believed to be responsible for the increased H_2 adsorption capacity on $Ce_xZr_{1-x}O_2$ when x is $\leqslant 0.5$ (Table 1; Fig. 12). When x is >0.5, the fraction of Ce^{4+}–O–Zr^{4+} centers decreases as the fraction of Ce^{4+}–O–Ce^{4+} centers increases. The protons associated with Ce^{3+}–O(H)–Zr^{4+} are more highly Brønsted-acidic

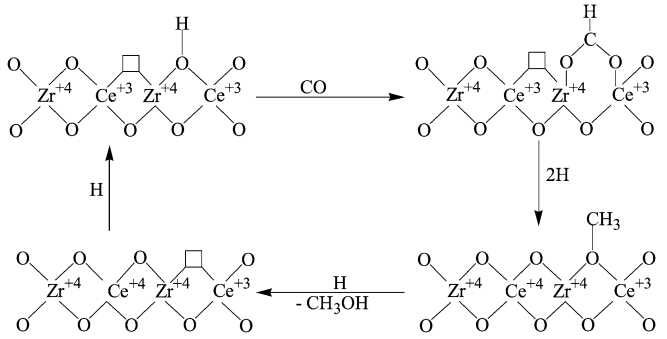

Scheme 1. Proposed reaction scheme of CO hydrogenation to methanol on $Cu/Ce_xZr_{1-x}O_2$.

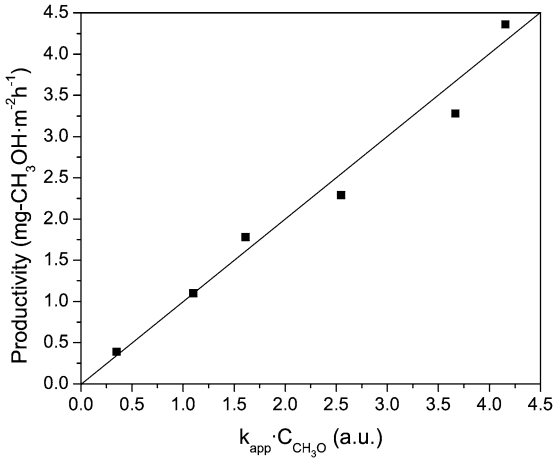

Fig. 11. Productivity vs. the product of k_{app} and surface methoxide concentration. Values of $k_{app} \times C_{CH_3O}$ are normalized to the value of 1.1 for 3 wt% Cu/ZrO_2

than those present as Zr^{4+}–O(H)–Zr^{4+}, which are known to be amphoteric, or those present as Ce^{3+}–O(H)–Ce^{4+} [40]. The higher Brønsted acidity of Ce^{3+}–O(H)–Zr^{4+} species and the higher absolute concentration of such species is hypothesized to be responsible for the increased rate of formate species hydrogenation to methoxide species (Fig. 10a) and the higher rate of methoxide removal as methanol (Fig. 10b). Thus, the incorporation of Ce cations into the framework of ZrO_2 enhances the adsorption of CO and to a greater extent the adsorption of H_2. The higher concentration of bridging hydroxyl species on the surface of $Ce_xZr_{1-x}O_2$ and, in particular, the higher Brønsted acidity of Ce^{3+}–O(H)–Zr^{4+} species are believed to be the primary origins of the higher activity of 3 wt% $Cu/Ce_xZr_{1-x}O_2$ seen in this study. Scheme 1 also provides a rational explanation for the observed maximum in the area-based methanol activity when $x = 0.5$.

The relationship between the steady-state rate of methanol synthesis and the transient-response data can now be examined. Assuming that the steady-state rate of methanol formation, r_{CH_3OH}, is equal to the rate of methoxide elimination from the surface of $Ce_xZr_{1-x}O_2$, r_{CH_3OH} can be expressed as $k_{app}C_{CH_3O}$ (Table 3), where C_{CH_3O} is the surface concentration of methoxide species at the start of the transient. The relative magnitude of C_{CH_3O} was estimated based on the area of IR bands in the 1200–1000 cm^{-1} range of surface methoxide species. Fig. 11 shows that r_{CH_3OH} is linearly related to $k_{app}C_{CH_3O}$, in agreement with the aforementioned assumption. The value of k_{app} is not constant, however; as shown in Table 3, it passes through a maximum as x increases from 0 to 1.0. One explanation for the variation in k_{app} is that it is due to the influence of x on the surface concentration of Brønsted acid protons of the form Ce^{3+}–O(H)–Zr^{4+}. The surface concentration of such protons is estimated by assuming that $k_{app} = k_{int}C_{OH}$, where k_{int} is the intrinsic rate coefficient for the reaction of Brønsted acid protons with methoxide groups and C_{OH} is the concentration of Brønsted acid protons on the surface of $Ce_xZr_{1-x}O_2$. If k_{int} is independent of x, then k_{app} should vary with x as a consequence of the dependence of C_{OH} on x. This hypothesis cannot be tested directly, however, because C_{OH} was not measured. However, Fig. 12 does show that k_{app} and the H_2 adsorption capacity of 3 wt% $Cu/Ce_xZr_{1-x}O_2$ depend on x in a very sim-

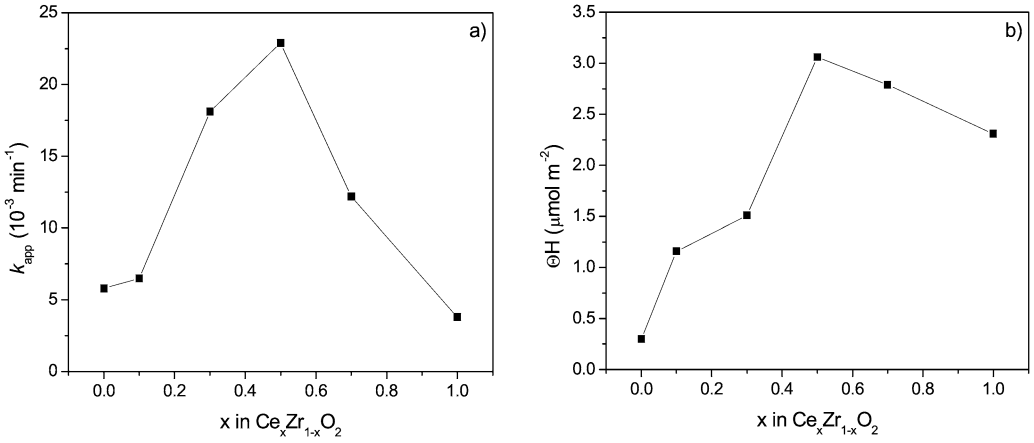

Fig. 12. Effect of cerium doping into ZrO_2 on (a) the first order apparent rate constant, k_{app}, and (b) hydrogen storage capacity.

ilar manner. Thus, it is reasonable to conclude that the surface concentration of Brønsted acid protons increases in a manner similar to the overall H_2 adsorption capacity of the catalyst.

5. Conclusions

The progressive substitution of Ce into the lattice zirconia leads to an increase in the area-based methanol synthesis activity of 3 wt% $Cu/Ce_xZr_{1-x}O_2$, which passes through a maximum for $x = 0.5$. The maximum in methanol synthesis activity is paralleled by a maximum in the hydrogen adsorption capacity of the catalyst. This latter effect is attributed to the formation of Ce^{3+}–O(H)–Zr^{4+} species by dissociative adsorption of H_2 on particles of supported Cu, followed by spillover of atomic H onto the oxide surface and reaction with Ce^{4+}–O–Zr^{4+} centers. The higher concentration of Ce^{3+}–O(H)–Zr^4 species on the oxide surface, together with the higher Brønsted acidity of these species, appears to be the primary cause of the fourfold-higher activity of 3 wt% $Cu/Ce_{0.5}Zr_{0.5}O_2$ relative to 3 wt% Cu/ZrO_2.

Acknowledgments

This work was supported by the Director, Office of Basic Energy Sciences, Chemical Sciences Division of the US Department of Energy under contract DE-AC02-05CH11231. Portions of this research were carried out at the Stanford Synchrotron Radiation Laboratory (SSRL), a national user facility operated by Stanford University on behalf of the US Department of Energy, Office of Basic Energy Sciences. The SSRL Structural Molecular Biology Program is supported by the Department of Energy, Office of Biological and Environmental Research, and by the National Institutes of Health, National Center for Research Resources, Biomedical Technology Program.

References

[1] B. Denise, R.P.A. Sneeden, Appl. Catal. 28 (1986) 235.
[2] Y. Sun, P.A. Sermon, J. Chem. Soc. Commun. (1993) 1242.
[3] Y. Sun, P.A. Sermon, Catal. Lett. 29 (1994) 361.
[4] I.A. Fisher, H.C. Woo, A.T. Bell, Catal. Lett. 44 (1997) 11.
[5] Y.W. Suh, S.H. Moon, H.K. Rhee, Catal. Today 63 (2000) 447.
[6] M.D. Rhodes, A.T. Bell, J. Catal. 233 (2005) 198.
[7] M.D. Rhodes, K.A. Pokrovski, A.T. Bell, J. Catal. 233 (2005) 210.
[8] K.A. Pokrovski, M.D. Rhodes, A.T. Bell, J. Catal. 235 (2005) 368.
[9] R.E. Jentoft, S.E. Deutsch, B.C. Gates, Rev. Sci. Instrum. 67 (1996) 211.
[10] M. Newville, J. Synchrotron Rad. 8 (2001) 322.
[11] B. Ravel, M. Newville, J. Synchrotron Rad. 12 (2005) 537.
[12] R.F. Hicks, C.S. Kellner, B.J. Savatsky, W.C. Hecker, A.T. Bell, J. Catal. 71 (1981) 216.
[13] H. Toraya, M. Yashmura, S. Somiya, J. Am. Ceram. Soc. 67 (1984) C–119.
[14] G. Colon, M. Pijolat, F. Valdivieso, H. Vidal, J. Kašpar, E. Finocchio, M. Daturi, C. Binet, J.C. Lavalley, R.T. Baker, S. Bernal, J. Chem. Soc., Faraday Trans. 94 (1998) 3717.
[15] C. Schild, A. Wokaun, R.A. Koeppel, A. Baiker, J. Catal. 130 (1991) 657.
[16] M. Li, Z. Feng, G. Xiong, P. Ying, Q. Xin, C. Li, J. Phys. Chem. B 105 (2001) 8107.
[17] C. Li, M. Li, J. Raman Spectrosc. 33 (2002) 301.
[18] A. Trovarelli, F. Zamar, J. Lorca, C. Leitenburg, G. Dolcetti, J.T. Kiss, J. Catal. 169 (1997) 490.
[19] V.S. Escribano, E.F. López, M. Panizza, C. Resini, J.M.G. Amores, G. Busca, Solid State Sci. 5 (2003) 1369.
[20] M. Yashima, H. Arashi, M. Kakihana, M. Yoshimura, J. Am. Ceram. Soc. 77 (1994) 1067.
[21] P. Fornasiero, G. Balducci, R. Di Monte, J. Kašpar, V. Sergo, G. Gubitosa, A. Ferrero, M. Graziani, J. Catal. 164 (1996) 173.
[22] S. Enzo, F. Delogu, R. Frattini, A. Primavera, A. Trovarelli, J. Mater. Res. 15 (2000) 1538.
[23] M. Shimokawabe, H. Asakawa, N. Takezawa, Appl. Catal. 59 (1990) 45.
[24] R. Zhou, T. Yu, X. Jiang, F. Chen, X. Zheng, Appl. Surf. Sci. 148 (1999) 263.
[25] M. Boaro, M. Vicaro, C. de Leitenburg, G. Dolcetti, A. Trovarelli, Catal. Today 77 (2003) 407.
[26] A. Trovarelli, G. Dolcetti, C. de Leitenburg, J. Kašpar, P. Finetti, A. Santoni, J. Chem. Soc., Faraday Trans. 88 (1992) 1311.
[27] C. de Leitenburg, A. Trovarelli, J. Kašpar, J. Catal. 166 (1997) 98.
[28] M. Boaro, M. Vicaro, C. de Leitenburg, G. Dolcetti, A. Trovarelli, Catal. Today 77 (2003) 407.
[29] J. Livage, Catal. Today 41 (1998) 3.
[30] C. Binet, M. Daturi, J.C. Lavalley, Catal. Today 50 (1999) 207.
[31] C. Binet, M. Daturi, J.C. Lavalley, J. Phys. Chem. 98 (1994) 6392.
[32] A. Badri, C. Binet, J.C. Lavalley, J. Chem. Soc., Faraday Trans. 93 (1992) 1159.
[33] C. Binet, M. Daturi, Catal. Today 70 (2001) 155.
[34] M.Y. He, J.G. Ekerdt, J. Catal. 87 (1984) 381.
[35] D. Bianchi, T. Chafik, M. Khalfallah, S.J. Teichner, Appl. Catal. A: Gen. 105 (1993) 223.
[36] C. Li, Y. Sakata, T. Arai, K. Domen, K. Maruya, T. Onishi, J. Chem. Soc., Faraday Trans. I 85 (1989) 1451.
[37] C. Lamonier, A. Ponchel, A. D'Huysser, L. Jalowiecki-Duhamel, Catal. Today 50 (1999) 247.
[38] J.L.G. Fierro, J. Soria, J. Sanz, J.M. Rojo, J. Solid State Chem. 66 (1987) 154.
[39] K.D. Jung, A.T. Bell, J. Catal. 193 (2000) 207.
[40] K. Tanabe, Solid Acids and Bases; Their Catalytic Properties, Academic Press, New York, 1970.